Isotope effect on confinement unraveled for L-mode in dimensionless $\rho_\star$ scan

P. A. Schneider[1], A. Bustos[2], P. Hennequin[3], F. Ryter[1], M. Bernert[1], M. Cavedon[1], M. G. Dunne[1], R. Fischer[1], T. Görler[1], T. Happel[1], V. Igochine[1], B. Kurzan[1], R. M. McDermott[1], P. Morel[3], M. Willensdorfer[1], the ASDEX Upgrade Team[1] and the EUROfusion MST1 Team*

[1]Max-Planck-Institut für Plasmaphysik, Boltzmannstr. 2, 85748 Garching, Germany
[2]Departamento de Física, Universidad Carlos III de Madrid, 28911 Leganés, Madrid, Spain
[3]Laboratoire de Physique des Plasmas, Ecole Polytechnique, France

Introduction: For predictions towards future fusion devices it is particularly important to understand the impact of the normalized gyroradius $\rho_\star = \rho/a$ on the confinement. In addition to the machine size a the main ion mass of the plasma is a parameter that will change from today's experiments. While today mainly pure deuterium (D) plasmas are studied, a fusion plasma will have significant fractions of tritium and helium. To understand the impact of the mass of the hydrogen (H) isotope on the plasma confinement many studies have been performed in the past. Typically, H plasmas are found with lower confinement than D [1, 2] albeit the opposite is expected by gyro-Bohm scaling of the transport coefficients which is well established in mono-isotope studies [3, 4]. Different theoretical explanations have been brought forward which focus on microscopic effects [5–7] or the pedestal stability in H-mode was discussed [8]. However, no satisfactory theoretical explanation for all observed phenomena is at present available.

This contribution focuses on macroscopic effects and the core transport. It is important to separate these from edge effects. In particular, ELMs behave significantly different when changing the main ion mass and the gas fuelling to achieve a density match [8,9]. It was also shown recently that the amount of ELM energy losses can impact the pedestal and thereby the confinement [10]. Therefore, an L-mode scenario was chosen to remove the impact of pedestal stability on the confinement. The main experiments consist of a dimensionless $\rho_\star$ scan in ECRH heated L-modes via an isotope scan using H and D plasmas. The dimensionless scan was chosen to minimize the impact of $\nu_\star$, β, L_T, L_n and the Mach number and allow to identify the influence the mass number has on transport and confinement.

Experimental Setup: The experimental strategy is to achieve a match in the kinetic profiles for two discharges with different hydrogen isotopes as main ions. The L-mode discharges described in the remainder of this section are AUG#30693 with D and AUG#31369 with H as main gas. These discharges are very reproducible which was demonstrated by running a series of similar discharges for each species. At a given density the heating power and thereby the temperature is limited by the prerequisite to stay in L-mode. The discharges were run with a plasma current of $I_\mathrm{p} = 0.80$ MA and a toroidal field of $B_\mathrm{t} = -2.46$ T resulting in a safety factor of $q_{95} = 5.07$.

*see http://www.euro-fusionscipub.org/mst1

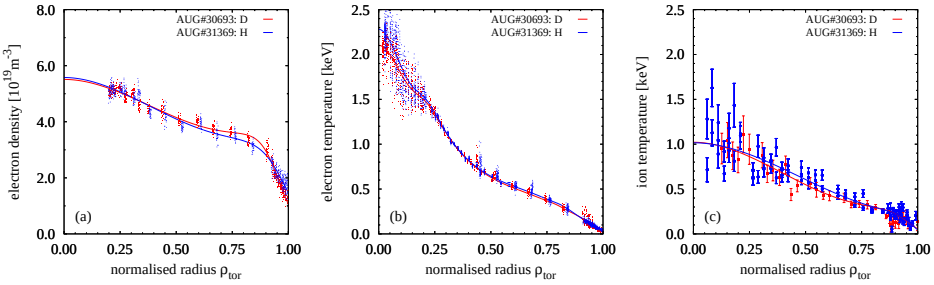

FIG. 1: Radial profiles of electron density (a), electron temperature (b) and ion temperature (c) for the discharge in deuterium (red) and in hydrogen (blue). The fits used for the modeling are indicated by solid lines.

A near perfect profile match was achieved with only electron cyclotron resonance heating (ECRH) as an auxiliary heating source. The mean ECRH heating power was 0.50 MW for D and 0.81 MW for H. The profiles of n_e, T_e and T_i are illustrated in figure 1. Adding the ohmic heating and taking the slightly different core radiation levels into account the power transported over the separatrix is $P^{D}_{sep} = 1.06$ MW and $P^{H}_{sep} = 1.39$ MW. This means the same stored energy in the plasma is achieved with $P^{D}_{sep} = 0.76 P^{H}_{sep}$. This ratio is similar to expectations from the empirical scalings. In fact, the discharge with H main ions performs 10% better compared to the scaling: $H^{D}_{98(y2)} = \tau^{D}_{E}/\tau_{E,98(y2)} = 0.67$, $H^{H}_{98(y2)} = 0.77$, $L^{D} = \tau^{D}_{E}/\tau_{E,L} = 1.02$, $L^{H} = 1.16$ [4, 11].

The discharges described above are matched in $\nu_\star$, β, L_T, L_n and ω_{tor} within the uncertainties. Differences in the radiation are taken into account for the modeling. The impact of the sawteeth on the heat flux is treated with the TRANSP sawtooth model which is based on the Kadomtsev principle.

Transport Analysis: The transport analysis is divided into three parts: two types of data interpretation (power balance and heat pulse transport analysis) and one theoretical consideration using gyrokinetic simulations.

The main tool for the power balance analysis is the TRANSP code [12]. It is used to determine the heat flux profiles for electrons q_e and ions q_i. Most relevant for the transport properties is $\rho_t > 0.3$ where $q^{H}_{e} = q^{D}_{e}$ and $q^{H}_{i} > q^{D}_{i}$. Although only electron heating is applied the heat fluxes are regulated by the electron-ion heat exchange term which is two times stronger in H compared to D. Therefore, the additional electron heating in H is in fact transported by the ion channel. There are three direct results from this power balance analysis. First, q_i shows no gyro-Bohm dependence because for the gyro-Bohm scaling $\sqrt{2} q^{H}_{i} = q^{D}_{i}$ would is expected. Second, the electron temperature is not affected by the changes in the ions. Third, $\rho_\star$ or the isotope mass is not the only parameter that changed in the experiment, the ion heat flux changed as well with $q^{H}_{i}/q^{D}_{i} = 1.5$ at $\rho_t = 0.6$. The resulting diffusivities are varying over the radius with $\chi^{PB}_{e} = 0.5 - 1.0$ m^2/s and $\chi^{PB}_{i} = 1 - 3$ m^2/s.

The heat pulse analysis using localised modulated ECRH to determine transient transport properties is a well established method [13, 14]. The ECRH is modulated at 100 Hz to induce small perturbations and their response in the electron temperature is measured with the ECE diagnostic. The Fourier analysis of the temperature perturbation yields radial amplitude A and phase ϕ profiles as shown in figure 2. The resulting diffusivities are calculated after [15, 16] and are $\chi^{HP}_{e,H} = 2.4 \pm 0.9$ m^2/s and $\chi^{HP}_{e,D} = 2.2 \pm 0.3$ m^2/s. This supports the results of the power balance analysis that H and D plasmas show the same electron heat transport for matched $\rho_{e\star}$ despite different $\rho_{i\star}$.

The expected microturbulent composition of the plasma is determined via linear and nonlinear gyrokinetic flux tube simulations using the GENE code [17]. These three species

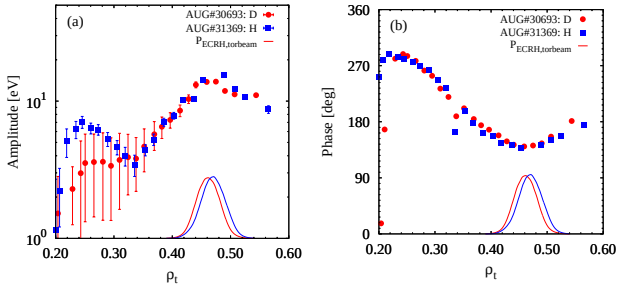

FIG. 2: Radial profiles for amplitude (a) and phase (b) of temperature perturbations. The ECRH deposition profile obtained from TORBEAM calculations is indicated with solid lines.

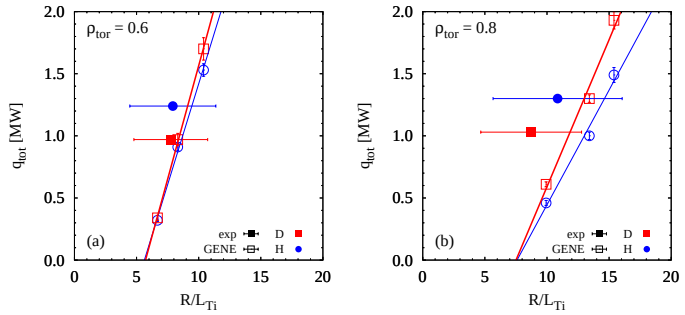

FIG. 3: Total heat fluxes plotted against the inverse ion temperature gradient length for two different radii. Open symbols show nonlinear GENE simulations and full symbols experimental measurements.

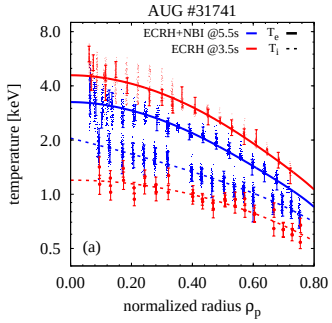

FIG. 4: Temperature profiles for phases with dominant electron heating (red) and dominant ion heating (blue). The case with ion heating has 15% lower confinement than the electron heated case.

simulations (ions, electrons and impurities) include electromagnetic effects, collisions and the macroscopic E×B shear flow present in AUG. To understand the trends resulting from gyrokinetics an arbitrary scan of the ion temperature gradient length $L_{T\mathrm{i}} = (\nabla(\ln T_\mathrm{i}))^{-1}$ was performed around the experimental data. Gradient scans in linear simulations suggest negligible influence of $L_{T\mathrm{e}}$ and L_n on the outcome of the nonlinear simulation. The ion temperature gradient (ITG) drive is the dominant turbulent mechanism for these discharges.

The main result of the $L_{T\mathrm{i}}$-scan is shown in figure 3 with the experimental measurements for two different radial positions in the plasma. In figure 3 the total heat fluxes $q_\mathrm{tot} = q_\mathrm{e} + q_\mathrm{i}$ are plotted against $1/L_{T\mathrm{i}}$. The implications of these GENE simulations are a high stiffness of the ion temperature. The heat fluxes do not follow gyro-Bohm theory because $q^\mathrm{D} < \sqrt{2}q^\mathrm{H}$ and they also do not follow the experimental trend $q^\mathrm{H} > q^\mathrm{D}$. However, within the uncertainties the simulated fluxes are still compatible with the experimental ones. If the total heat fluxes are matched with the experimental ones, GENE predicts a distribution for the heat fluxes of $q_\mathrm{i}/q_\mathrm{e} \sim 1.5 \ldots 2.5$. This ratio is consistent with the experimental data regarding the observation of additional heat flux being transported over the ion channel.

Impact of $q_\mathrm{i}/q_\mathrm{e}$: In the previous section it was discussed that the dimensionless $\rho_\star$ scan was achieved with constant q_e and a variation in q_i. To separate the influence of mass and ion heat flux, additional experiments were performed. The aim was to achieve an identity match in the same gas with different heating methods. One discharge was the pure electron heated AUG#30693 discussed above and the second discharge AUG#33708 used direct ion heating $P_\mathrm{NBI} = 0.56$ MW and $P_\mathrm{ECRH} = 0.16$ MW.

The first striking observation is that $P_\mathrm{sep}^\mathrm{D,NBI} = 1.24$ MW is necessary for a profile

match which is $P_{\rm sep}^{\rm D,ECRH}/P_{\rm sep}^{\rm D,NBI} = 0.85$. The density profile is less peaked and the NBI torque results in a slightly faster toroidal plasma rotation. Still this observation can be understood considering $L_{T\rm e} \neq L_{T\rm i}$ and assuming strong profile stiffness for both channels. Getting more heat into the channel with the lower $L_{\rm T}^{-1}$ will result in reduced confinement. This is a direct consequence of the profile stiffness and does not require a change in the underlying transport mechanism. This concept is confirmed with a change of electron vs. ion heating mix during individual discharges for both H and D plasmas. An example is shown in figure 4 in logarithmic scale to illustrate the gradient lengths. The response of edge plasma temperature was the same for electrons and ions - so with $L_{T\rm i} = L_{T\rm e}$ the confinement would have been the same.

Discussion: Experiments are performed to explore the impact of $\rho_\star$ and ion mass on the core confinement. To analyse core transport effects the impact of the edge plasma is minimized. In particular, ELMs are avoided by choosing an L-mode scenario.

The dimensionless mass- or $\rho_\star$-scan reveals that the lower confinement in H compared to D plasmas is accompanied by a larger ion heat flux due to the enhanced electron ion heat transfer. The electron transport channel is unaffected by the different main ion mass, as indicated by both power balance and heat pulse transport analysis. A significant impact on the electron temperature in these ITG dominated discharges is also not expected from nonlinear GENE simulations. These simulations highlight the importance of the ion heat transport channel. By scanning $R/L_{T\rm i}$ a heat flux match can be achieved by varying the experimental gradients within their uncertainties. Unfortunately, the uncertainties in the ion temperature measurements are too large for a stronger conclusion.

Additional experiments with the same isotope mass show that larger ion heat fluxes - due to direct ion heating - will lead to reduced confinement when $R/L_{T\rm i} < R/L_{T\rm e}$ for stiff temperature profiles and when the type of transport is not changed by the different heating. In the presented experiments the heating power necessary to achieve the same stored energy scales linearly with $\langle q_{\rm i}/q_{\rm e}\rangle$ or $\tau_{\rm E}^{-1} \propto \langle q_{\rm i}/q_{\rm e}\rangle$ regardless of the main ion mass. This means, for the ITG dominated L-modes discussed here, the impact of the isotope mass on $p_{\rm ei}$ is sufficient to explain the degradation of confinement. In particular, we find that in this situation $\tau_{\rm E}$ is not suited to describe the underlying transport physics.

This work has been carried out within the framework of the EUROfusion Consortium and has received funding from the Euratom research and training programme 2014-2018 under grant agreement No 633053. The views and opinions expressed herein do not necessarily reflect those of the European Commission.

[1] STAMBAUGH, R. et al., Plasma Physics and Controlled Fusion **30** (1988) 1585.
[2] BESSENRODT-WEBERPALS, M. et al., Nuclear Fusion **33** (1993) 1205.
[3] WALTZ, R. E. et al., Physical Review Letters **65** (1990) 2390.
[4] ITER Physics Expert Group, Nuclear Fusion **39** (1999) 2137.
[5] BUSTOS, A. et al., Physics of Plasmas **22** (2015) .
[6] GURCHENKO, A. D. et al., Plasma Physics and Controlled Fusion **58** (2016) 44002.
[7] HENNEQUIN, P. et al., Comprehensive experimental study of plasma turbulence structure and its scaling with $\rho_\star$, in *42th EPS Conference on Plasma Physics*, page I1.102, Lisbon, 2015.
[8] URANO, H. et al., Nuclear Fusion **53** (2013) 83003.
[9] SCHISSEL, D. P. et al., Nuclear Fusion **29** (1989) 185.
[10] SCHNEIDER, P. A. et al., Plasma Physics and Controlled Fusion **57** (2015) 14029.
[11] KAYE, S. M. et al., Nuclear Fusion **37** (1997) 1303.
[12] HAWRYLUK, R. J., An Empirical Approach to Tokamak Transport, in *Phys. Plasmas Close Thermonucl. Cond.*, volume 1, page 19, 1980.
[13] IMBEAUX, F. et al., Plasma Physics and Controlled Fusion **43** (2001) 1503.
[14] RYTER, F. et al., Nuclear Fusion **43** (2003) 1396.
[15] LOPES-CARDOZO, N. J. et al., Plasma Physics and Controlled Fusion **32** (1990) 983.
[16] JACCHIA, A. et al., Physics of Fluids B **3** (1991).
[17] JENKO, F. et al., Physics of Plasmas **7** (2000) 1904.